SAND2019-7333J

Elucidating Structure-Spectral Properties Relationships of Negative Thermal Expansion $Zr_2(WO_4)(PO_4)_2$: A First-Principles Study with Experimental Validation

Philippe F. Weck[*,†], Eunja Kim[‡], Margaret E. Gordon[†], Jeffery A. Greathouse[†], Stephen P. Meserole[†], and Charles R. Bryan[†]

[†] Sandia National Laboratories, Albuquerque, New Mexico 87185, United States

[‡] Department of Physics and Astronomy, University of Nevada Las Vegas, 4505 Maryland Parkway, Las Vegas, Nevada 89124, United States

ABSTRACT: The phonon, infrared and Raman spectroscopic properties of zirconium tungsten phosphate, $Zr_2(WO_4)(PO_4)_2$ (space group *Pbcn*, IT No. 60; $Z = 4$), have been extensively investigated using density functional perturbation theory (DFPT) calculations with the Perdew, Burke and Ernzerhof exchange-correlation functional revised for solids (PBEsol), and validated by experimental characterization of $Zr_2(WO_4)(PO_4)_2$ prepared by hydrothermal synthesis. Using DFPT-simulated infrared, Raman, and phonon density-of-state spectra combined with FT-IR and Raman measurements, new comprehensive and extensive assignments have been made for the spectra of $Zr_2(WO_4)(PO_4)_2$, resulting in the characterization of its 29 and 34 most intense IR- and Raman-active modes, respectively. DFPT results also reveal that $\nu_1(PO_4)$ symmetric stretching and $\nu_3(PO_4)$ antisymmetric stretching bands have been interchanged in previous Raman experimental assignments. Negative thermal expansion (NTE) in $Zr_2(WO_4)(PO_4)_2$ appears to have very limited impact on the spectral properties of this compound. This work shows the high accuracy of the PBEsol exchange-correlation functional for studying the spectroscopic properties of crystalline materials using first-principles methods.

1. INTRODUCTION

Over the last few decades, negative thermal expansion (NTE) has been observed in several materials in the Zr/W/O, Zr/V/P/O, and Zr/W/P/O systems.[1,2,3,4,5,6,7,8,9,10,11,12,13,14,15,16,17,18] Such NTE materials are crucial as thermal-expansion compensators in composites designed to have overall zero or adjustable thermal expansion. Relevant technological applications include, for example, high-precision optical systems, high-performance thermoelectric converters, nanoscale semiconductor devices, or fuel cells.[19,20,21,22,23,24,25,26,27]

Among Zr/W/P/O crystalline phases, the NTE compound zirconium tungsten phosphate, with formula $Zr_2(WO_4)(PO_4)_2$, has been the focus of much experimental attention. First synthesized by Martinek and Hummel[28] and characterized by Tsvigunov and Sirotinkin,[29] the crystal structure of $Zr_2(WO_4)(PO_4)_2$ was fully solved by Evans *et al.*[30] using room-temperature powder X-ray diffraction (XRD) techniques. Its structure adopts the orthorhombic space group *Pbcn* (IT No. 60; $a = 9.35451(9)$, $b = 12.31831(9)$, $c = 9.16711(8)$ Å; $Z = 4$) and consists of corner-sharing ZrO_6 octahedral and WO_4/PO_4 tetrahedral coordination units. $Zr_2(WO_4)(PO_4)_2$ was the first reported crystalline phase with coexistence of WO_4 and PO_4 coordination and is closely related to compounds $A_2(MO_4)_3$ (A = Al, Sc, Cr, Fe, Y, In, Ho, Er, Tm, Yb, Lu, and M = Mo; or A = Al, Sc, Fe, In, Y, Gd, Tb, Dy, Ho, Yb, Tm, Yb, Lu, and M = W). Members of the $A_2(MO_4)_3$-type crystallize either in the orthorhombic *Pbcn*/*Pnca* or $P2_1/a$ space groups. As in ZrW_2O_8-type systems, NTE behavior in $A_2(MO_4)_3$-type structures originates from the transverse thermal motion of bridging O atoms in A−O−M, as shown by Evans et al.[31] Previous XRD and dilatometer investigations at atmospheric pressure revealed that orthorhombic $Zr_2(WO_4)(PO_4)_2$ features NTE behavior from below room-temperature up to 1373 K.[31,32,33,34,35,36] In particular, the absence of phase transition in $Zr_2(WO_4)(PO_4)_2$ at ambient pressure is generally regarded as highly desirable, compared to other well-known NTE compounds, such as the low-temperature α-ZrW_2O_8 (space group $P2_13$), which transforms into the β-ZrW_2O_8 phase (space group $Pa\overline{3}$) above 431 K.[2,4,11] For this reason, $Zr_2(WO_4)(PO_4)_2$ has often been utilized to stabilize other NTE materials in the design of various NTE composites, such as $Zr_2(WO_4)(PO_4)_2/ZrW_2O_8$ or $Zr_2(WO_4)(PO_4)_2/ZrV_{0.6}P_{1.4}O_7$.[37,38,39]

However, a major hindrance for the wider application of $Zr_2(WO_4)(PO_4)_2$ has remained the synthesis of this material with consistent NTE properties. Indeed, previous experimental studies showed that the different porosities and average grain sizes resulting from sintering conditions and/or synthesis reactions[31,32,33,34,35,36] or pressure-induced phase transformations[40] during $Zr_2(WO_4)(PO_4)_2$ fabrication can lead to significant variations in its coefficient of thermal expansion (CTE). For example, mean linear CTE values of -6×10^{-6} and -3×10^{-6} K were measured in the temperature range 50−450 K by Evans and coworkers[31] using dilatometer and XRD measurements, while values of -5×10^{-6} K and -3.4×10^{-6} K were obtained by Cetinkol and Wilkinson[33] from neutron diffraction data between 60−300 K and by Isobe et al.[32] in the range 300−875 K, respectively.

Most of the aforementioned experimental studies of $Zr_2(WO_4)(PO_4)_2$ focused on its NTE behavior, with only extremely limited data available on its spectroscopic and vibrational properties. The recent Raman spectra collected by Yuan et al.[41] on samples pre-sintered at 1573 K revealed vibrational modes at *ca*. 407, 425, 830, 868, 1019 and 1097 cm^{-1}, although the actual material characterized was a mixture of $Zr_2(WO_4)(PO_4)_2$ and WO_3. Moreover, as mentioned in the recent review by Dove and Fang,[27] few computational studies have been devoted to NTE materials. To the best of our knowledge, the first computational investigation of the orthorhombic phase of $Zr_2(WO_4)(PO_4)_2$ was conducted by Weck et al.[42], and focused on predicting the structural, mechanical and thermodynamic properties of this material within the framework of density functional perturbation theory (DFPT) using the exchange-correlation (XC) functional parameterized by Perdew, Burke and Ernzerhof for solids (PBEsol).[43]

In this work, the vibrational properties and phonon density-of-state (PDOS), infrared (IR), Raman spectra of $Zr_2(WO_4)(PO_4)_2$ have been systematically investigated with DFPT. To assess the validity and accuracy of the present DFPT results, an extensively comparison was carried out with Fourier transform infrared (FT-IR) and Raman data generated in this study and the previous Raman measurements reported by Yuan et al.[41] The DFPT linear-response methodology, using the PBEsol XC functional, adopted in previous first-principles studies[42,44,45] of NTE $Zr_2(WO_4)(PO_4)_2$ and α-ZrW_2O_8 was utilized in this investigation. DFPT methods are regarded as more effective than standard DFT finite-displacements approaches utilized to determine the vibrational properties of many-particle systems, since additional physical properties (e.g., IR and Raman absorbance) can be derived from the total energy with respect to perturbations.[46] Numerous lattice dynamics studies previously tested the accuracy of such DFPT methods.[42,44,45,47,48,49,50,51,52]

Details of our computational and experimental methods are given in the Section 2, followed by the analysis and discussion of our results in Section 3, and a summary of our findings and conclusions in Section 4.

2. METHODS

Computational Methods. First-principles calculations were conducted using DFT/DFPT implemented in the Vienna *ab initio* simulation package (VASP).[53] The exchange-correlation energy was calculated using the generalized gradient approximation (GGA), with the PBEsol[43] parameterization. In previous computational studies of the NTE compound α-ZrW_2O_8,[42,44,45] the PBEsol XC functional showed superior accuracy over standard functionals. The present DFT/DFPT computational approach was extensively tested in previous lattice dynamics studies.[47,48,49,50,51,52]

The interaction between valence electrons and ionic cores was described by the projector augmented wave (PAW) method.[54,55] The Zr($4p^6$,$5s^2$,$4d^2$), W($6s^2$,$5d^4$), O($2s^2$,$2p^4$) and P($3s^2$,$3p^3$) electrons were treated as valence electrons in the Kohn-Sham (KS) equations and the remaining core electrons together with the nuclei were represented by PAW pseudopotentials. The blocked Davidson[56] iterative matrix diagonalization scheme was utilized to solve the KS equations. The plane-wave cutoff energy was set to 500 eV for the electronic wavefunctions, ensuring the total energy of the system to be converged to within 1 meV/atom.

The orthorhombic $Zr_2(WO_4)(PO_4)_2$ unit cell crystallizing in the space group *Pbcn* (IT No. 60, setting No. 3 *Pnca* (*c*, *a*, *b*); $Z = 4$, 68 atoms; $V_0 = 1056.34$ Å^3) characterized by Evans *et al.*[30] was used in initial structure relaxation calculations. A *k*-point mesh of 5×5×5 was utilized to sample the Brillouin zone using the Monkhorst-Pack *k*-point scheme[57]. Full relaxation calculations of the unit cell, without symmetry constraints imposed, were initially carried out until the Hellmann-Feynman forces acting on atoms were converged within 0.01 eV/Å. The equilibrium structure obtained from total-energy minimization was further optimized with respect to Hellmann-Feynman forces, with a convergence tolerance set to 0.001 eV/Å, and DFPT linear response calculations were carried out with VASP to determine the phonon frequencies and associated intensities. The latter were computed from the Born effective charges (BEC) tensor, which corresponds to the change in atoms polarizabilities with respect to an external electric field. IR and Raman spectra predicted with this method in previous computational studies of the NTE compound α-ZrW_2O_8 showed very good agreement with experimental spectroscopic data.[45] This DFPT approach was also utilized and tested in numerous previous investigations to successfully predict the properties of various Zr-containing compounds and crystalline materials.[47,48,49,50,58,59,60,61,62,63,64]

Experimental Methods. All reagents were used as received and were tested via thermogravimetric analysis to determine actual molar amounts of Zr, P, and W respectively. Based on the procedure reported by Shi *et al.*[36], the molar ratio Zr/P/W was held to 2:1:2 throughout the synthesis.

0.9021 g ammonium paratungstate $(NH_4)_{10}(H_2W_{12}O_{42})*xH_2O$ (Aldrich) was mixed with 30 mL DI H_2O. 1 g of ammonium phosphate monobasic (Aldrich), $NH_4H_2PO_4$, was mixed with 20 mL H_2O. These solutions were combined, covered, and stirred for a minimum of 60 min and up to 24 hours.

2.5271 g zirconyl oxychloride octahydrate (Aldrich) was mixed with 5mL DI H_2O and stirred until dissolved. This Zr solution was then slowly added dropwise to the phospho-tungsten solution while stirring. After an additional 90 minutes of stirring, the pH was measured using pH paper to be highly acidic (pH <1).

The solution was placed in a Teflon lined Parr vessel and placed in an oven at 130º C for 48 hours. Upon removal from the Parr vessel, the fine white precipitate was filtered and washed with DI water. After drying in an oven at 80 ºC overnight, the precipitate was fired in a 900ºC furnace for 4 hours, removed, and allow to cool to room temperature.

Infrared spectra were collected at room temperature using a Thermo Scientific Nicolet 6700 Fourier Transform Infrared (FT-IR) spectrometer and OMNIC 8.3 software suite fitted with a Nicolet Smart DuraSamplIR (single bounce diamond crystal) and used air as the background and blank. The powder was placed onto the diamond crystal and pressure was applied before spectra were collected. Scans were done on the sample at a resolution of 1 cm^{-1} over an absorbance range of 4000.12 to 525.02 cm^{-1}, using a KBr beamsplitter and a DTGS (deuterated triglycine sulfate) KBr detector with atmospheric and ATR corrections applied.

Raman spectra were collected at room temperature using a Horiba T64000 Raman Spectrometer fitted with 1800 grooves/mm gratings and a Symphony CCD detector and controlled with the Lab-Spec 5 software. A Coherent I90-5 Argon-ion laser (514.532 nm laser line set at 250 mW at the head) was used for excitation. The instrument was calibrated by analyzing a piece of silicon wafer (520.7 cm^{-1}). The $Zr_2(W_2O_4)(PO_4)_2$ spectrum shown was captured using 20 accumulations of 60 seconds. An Olympus BH2 (BHSM) microscope with a BH2-UMA fitted with a ULWD MS Plan 80 objective (NA= 0.75) was used for sampling the material. Data collection was done in the single mode between 99 to 1300 cm^{-1}.

3. RESULTS AND DISCUSSION

Crystal Structure. Figure 1 shows a ball-and-stick representation of the orthorhombic $Zr_2(WO_4)(PO_4)_2$ crystal unit-cell structure (space group *Pbcn*, IT No. 60, setting No. 3 *Pnca* (*c*, *a*, *b*); $Z = 4$) optimized at the GGA/PBEsol level of theory at $T = 0$ K. As described in the study of Evans et al.,[30] $Zr_2(WO_4)(PO_4)_2$ consists of corner-sharing ZrO_6 octahedral units, each connected to two WO_4 and four PO_4 tetrahedral coordination units. 8*d* Wyckoff sites (1 symmetry) are occupied by Zr, P and O atoms, while W atoms are positioned at 4*c* Wyckoff sites (.2. symmetry).

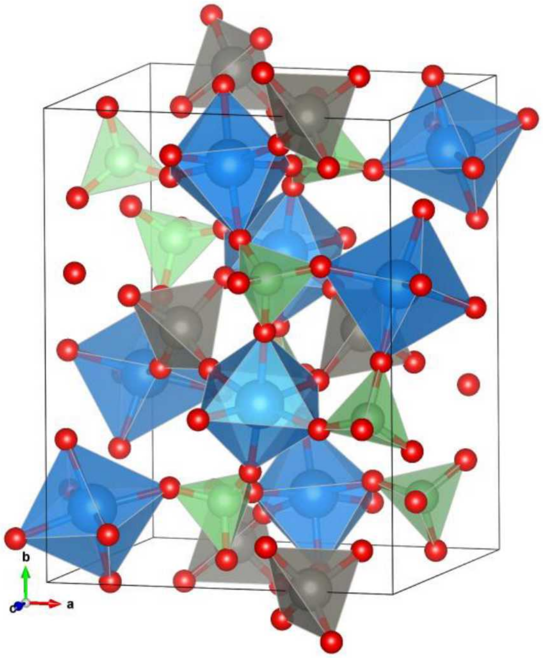

Figure 1. Crystal unit cell of $Zr_2(WO_4)(PO_4)_2$ (space group *Pbcn*, IT No. 60, setting No. 3 *Pnca* (*c*, *a*, *b*); $Z = 4$), with corner-sharing ZrO_6 octahedral (blue) and WO_4 (grey) and PO_4 (green) tetrahedral coordination units, optimized at the GGA/PBEsol level of theory. Color legend: O, red; P, green; W, grey; Zr, blue.

Figure 1 shows a ball-and-stick representation of the orthorhombic $Zr_2(WO_4)(PO_4)_2$ crystal unit-cell structure (space group *Pbcn*, IT No. 60, setting No. 3 *Pnca* (*c*, *a*, *b*); $Z = 4$) optimized at the GGA/PBEsol level of theory at $T = 0$ K. As described in the study of Evans et al.,[30] $Zr_2(WO_4)(PO_4)_2$ consists of corner-sharing ZrO_6 octahedral units, each connected to two WO_4 and four PO_4 tetrahedral coordination units. 8*d* Wyckoff sites (1 symmetry) are occupied by Zr, P and O atoms, while W atoms are positioned at 4*c* Wyckoff sites (.2. symmetry).

Table 1. Structural Parameters of the $Zr_2(WO_4)(PO_4)_2$ Unit Cell (space group *Pbcn*, IT No. 60; $Z = 4$) Calculated With DFT at the GGA/PBEsol Level and Measured From Neutron and Powder X-Ray Diffraction Data.

Method	*T*(K)	*a*(Å)	*b*(Å)	*c*(Å)	*V*($Å^3$)
DFT[a]	0	9.432	12.432	9.250	1084.59
Expt.[b]	60	9.3640(3)	12.3243(4)	9.1793(3)	1059.34(4)
Expt.[b]	296	9.3462(3)	12.3313(4)	9.1606(3)	1055.77(4)
Expt.[c]	300	9.35451(9)	12.31831(9)	9.16711(8)	1056.34

[a]This study. [b]Cetinkol and Wilkinson; ref. 33; Neutron diffraction. [c]Evans et al.; ref. 30; powder XRD.

The computed and measured unit-cell lattice parameters of $Zr_2(WO_4)(PO_4)_2$ are summarized in Table 1. The parameters of $a = 9.432$ Å, $b = 12.432$ Å and $c = 9.250$ Å ($b/a = 1.318$, $c/a = 0.981$, $V = 1084.59$ $Å^3$) predicted at the GGA/PBEsol level are in close agreement with the low-temperature ($T = 60$ K) neutron diffraction estimates of $a = 9.3640(3)$ Å, $b = 12.3243(4)$ Å and $c = 9.1793(3)$ Å ($b/a = 1.3161$, $c/a = 0.9803$, $V = 1059.34(4)$ $Å^3$) reported by Cetinkol and Wilkinson.[33] These DFT results are also consistent with the room-temperature powder XRD values of $a = 9.35451(9)$ Å, $b = 12.31831(9)$ Å and $c = 9.16711(8)$ Å ($b/a = 1.3168$, $c/a = 0.9800$, $V = 1056.34$ $Å^3$) obtained by Evans and coworkers.[30]

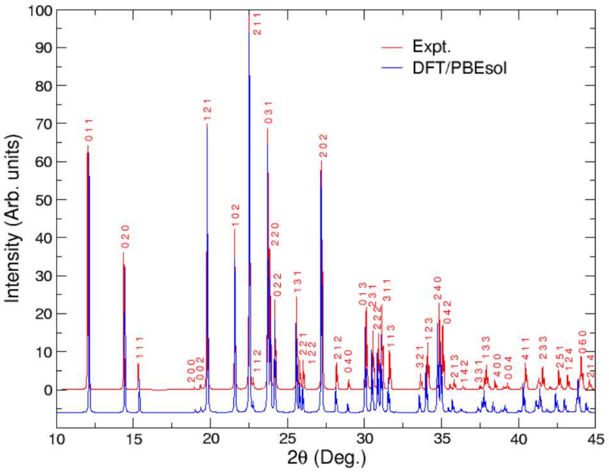

Figure 2. (a) Experimental room-temperature powder X-ray diffraction pattern of $Zr_2(WO_4)(PO_4)_2$ (Cu Kα radiation, $\lambda = 1.5406$ Å) (ref. 30) and (b) simulated XRD pattern for the crystal unit-cell optimized with DFT at the GGA/PBEsol level of theory. Observed reflections are indexed in the *hkl* representation.

The simulated XRD pattern (Cu Kα radiation, $\lambda = 1.5406$ Å) for the crystal structure optimized in this study at the GGA/PBEsol level of theory, without relaxation of the experimental crystal lattice[30], is displayed in Figure 2. Excellent overall agreement is obtained with the room-temperature powder XRD pattern of the orthorhombic $Zr_2(WO_4)(PO_4)_2$ structure reported by Evans *et al.*[30]. All the observed reflections, indexed in the *hkl* representation in Figure 2, are well reproduced, with very limited peak shift of 2θ values.

To further validate the accuracy of the $Zr_2(WO_4)(PO_4)_2$ structure optimized with GGA/PBEsol, an extensive comparison was made between computed and experimental interatomic structural parameters. Table 2 summarizes calculated and measured[30] bond distances and angles. Average bond distances are predicted to be 1.783 Å for W−O, 2.085 Å for Zr−O, and 1.537 Å for P−O, very close to the values of 1.799 Å, 2.087 Å and 1.500 Å measured by Evans and coworkers[30]. Tetrahedral O−W−O and O−P−O angles and octahedral O−Zr−O angles are near their ideal values of 109.5° and 90.0°, respectively, thus indicating limited distortion from perfect polyhedral coordination units (see Figure 1). The optimized ZrO_6 octahedral units and WO_4 and PO_4 tetrahedral units have volumes of 11.979 Å^3, 2.909 Å^3 and 1.863 Å^3, which compare well with the measured values of 11.995 Å^3, 2.820 Å^3 and 1.731 Å^3, respectively.

Let us note that these interatomic structural parameters for $Zr_2(WO_4)(PO_4)$ are also in line with our previous calculations for α-ZrW_2O_8 using GGA/PBEsol.[44] In the optimized structure of α-ZrW_2O_8, made of corner-sharing ZrO_6 octahedral coordination units and WO_4 tetrahedral units with distinct W1 and W2 metal centers, the average Zr−O, W1−O, and W2−O bond distances are 2.084 Å, 1.799 Å, and 1.787 Å, respectively. The predicted volumes for the ZrO_6 octahedral units and the $W1O_4$ and $W2O_4$ tetrahedral units are 12.115 Å^3, 2.872 Å^3, and 2.925 Å^3.[44]

Table 2. Bond Distances (Å) and Angles (°) of $Zr_2(WO_4)(PO_4)_2$ (Space Group *Pbcn*, IT No. 60; $Z = 4$) Calculated with DFT at the GGA/PBEsol Level and Measured Using Room Temperature Powder X-Ray Diffraction.

	O1	O2	O3	O4	O5	O6
W1[a]	1.784	1.784			1.783	1.783
W1[b]	1.728(13)	1.728(13)			1.806(12)	1.806(12)
Zr1[a]	2.141	2.038	2.063	2.051	2.167	2.049
Zr1[b]	2.186(13)	2.039(12)	2.045(12)	2.042(10)	2.149(13)	2.060(16)
P1[a]		1.537	1.531	1.537		1.543
P1[b]		1.491(12)	1.541(12)	1.514(12)		1.456(16)
O−W−O[a]	109.1	110.4	109.0			
O−W−O[b]	110.8(9)	111.8(6)	105.7(5)			
W−O−Zr[a]	169.8					
W−O−Z[b]	164.6(7)					
Zr−O−P[a]	155.9	175.0				
Zr−O−P[b]	155.7(8)	175.6(7)				
O−P−O[a]	110.4	108.9	108.7	109.2	109.6	109.9
O−P−O[b]	109.3(7)	109.9(8)	109.9(7)	107.8(7)	107.2(7)	112.5(8)

[a]This study. [b]Evans et al.; ref. 30; powder XRD. The same atom naming convention as in Ref. 30 is used in this study.

Table 3. Character Table for $Zr_2(WO_4)(PO_4)_2$ (Space Group *Pbcn*, IT No. 60, with 8*d* and 4*c* Wyckoff Sites Occupied).

Irreps[a]	Multiplicity[a]	*E*	2_z	2_y	2_x	*I*	m_z	m_y	m_x	Functions	IR Active[b]	Raman Active[b]
A_g	25	1	1	1	1	1	1	1	1	x^2,y^2,z^2	no	yes
B_{1g}	26	1	1	-1	-1	1	1	-1	-1	xy,J_z	no	yes
B_{2g}	25	1	-1	1	-1	1	-1	1	-1	xz,J_y	no	yes
B_{3g}	26	1	-1	-1	1	1	-1	-1	1	yz,J_x	no	yes
A_u	25	1	1	1	1	-1	-1	-1	-1	—	no	no
B_{1u}	26	1	1	-1	-1	-1	-1	1	1	z	yes	no
B_{2u}	25	1	-1	1	-1	-1	1	-1	1	y	yes	no
B_{3u}	26	1	-1	-1	1	-1	1	1	-1	x	yes	no

[a]Vibrational modes belonging to all the irreducible representations (irreps) are non-degenerate. [b]Vibrational modes belonging to the A_g, B_{1g}, B_{2g} and B_{3g} irreps are Raman active (quadratic functions), while modes from the B_{1u}, B_{2u} and B_{3u} irreps are IR active (linear functions), and modes from the A_u irrep are IR and Raman inactive.

Phonon, Infrared, and Raman Spectra. Forces exerted on all atoms of the equilibrium bulk structure of $Zr_2(WO_4)(PO_4)_2$ were calculated using DFPT at the GGA/PBEsol level and phonon frequencies were derived at the center of the Brillouin zone (Γ-point) for IR and Raman calculations. The resulting phonon density-of-states (PDOS) spectrum of $Zr_2(WO_4)(PO_4)_2$ calculated at $T = 0$ K is displayed in Figure 3, with a smearing width of $\sigma = 10$ cm^{-1} utilized to simulate the temperature effect in the PDOS. Since the PDOS of $Zr_2(WO_4)(PO_4)_2$ has yet to be measured, to the best of our knowledge, the PDOS of the α-ZrW_2O_8 compound previously calculated[45] with DFPT/GGA/PBEsol is also shown for comparison. As discussed in previous studies[4,13,45], a correlation can be established between the internal modes of vibrations of the WO_4 tetrahedral units in crystalline α-ZrW_2O_8 and an ideal, free tungstate ion, exhibiting high-frequency symmetric (ν_1) and antisymmetric (ν_3) stretching modes, and lower-frequency symmetric (ν_2) and antisymmetric (ν_4) bending modes. Similar correspondences exist between WO_4 and PO_4 tetrahedral units composing $Zr_2(WO_4)(PO_4)_2$ and isolated tungstate and phosphate ions. Since both α-ZrW_2O_8 and $Zr_2(WO_4)(PO_4)_2$ compounds possess WO_4 and ZrO_6 units, additional features in the PDOS of $Zr_2(WO_4)(PO_4)_2$ can be mainly ascribed to PO_4 modes of vibration. Previous experimental studies of $(AMO_4)_2$ (A = Zr, Hf; M = W, Mo) compounds suggested that the ν_1 and ν_3 stretching modes and ν_4 and ν_2 bending modes of WO_4 units typically lie within the ranges ~950−1032 cm^{-1}, ~750−950 cm^{-1}, ~320−400 cm^{-1} and ~280−320 cm^{-1}, respectively. [13,41,65] In their recent Raman study of $Zr_2(WO_4)(PO_4)_2$, Yuan et al. tentatively assigned the corresponding PO_4 modes of ν_1 symmetric stretching, ν_3 antisymmetric stretching and ν_4+ν_2 bending vibrations within the ranges ~1030−1200 cm^{-1}, ~1000−1030 cm^{-1}, and ~400−650 cm^{-1}, respectively.[41] However, as shown by previous experimental band assignments for zirconium phosphate ceramics, such as $Na_{1-x}(Cs_{1.33}Sr)_xZr_2P_3O_{12}$ (x = 0.1-1.0) or $Ca_{1-2x}Zr_4Mo_{2x}P_{6-2x}O_{24}$ (x = 0.1-0.5), ν_1, ν_3, ν_4, and ν_2 PO_4 bands are typically in the ranges ~900−990 cm^{-1}, ~1030−1260 cm^{-1}, ~510−640 cm^{-1} and ~400−500 cm^{-1}.[66] Vibrational spectroscopy characterization of phosphate minerals also indicate higher frequency for $\nu_3(PO_4)$ bands compared to $\nu_1(PO_4)$ bands.[67] Therefore, it appears that $\nu_1(PO_4)$ and $\nu_3(PO_4)$ bands might have been interchanged in the assignment made by Yuan et al.[41]

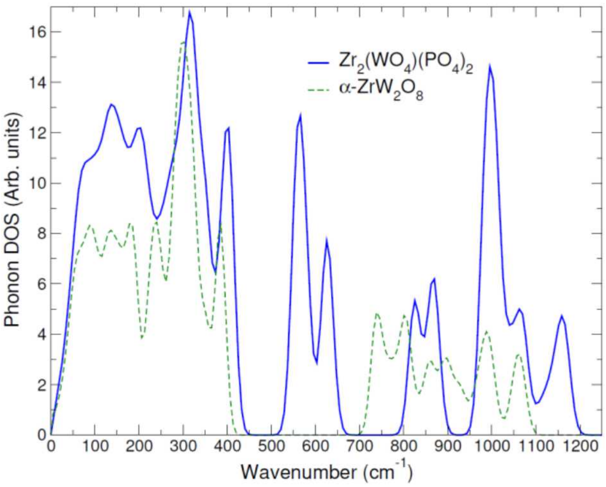

Figure 3. Phonon density-of-states (PDOS) spectra of $Zr_2(WO_4)(PO_4)_2$ (blue solid line) and α-ZrW_2O_8 (green dashed line) simulated using density functional perturbation theory (DFPT) at the GGA/PBEsol level. A smearing width of $\sigma = 10$ cm^{-1} was used to generate PDOS spectra.

As depicted in Figure 3, DFPT/PBEsol calculations for α-ZrW_2O_8 predicted ν_1 and ν_3 stretching modes of WO_4 units in the ranges 1013−1032 cm^{-1} and 739−992 cm^{-1}, respectively, with ν_4+ν_2 bending modes within 277−381 cm^{-1}, with libration, lattice and translation modes below $\omega \cong 256$ cm^{-1}.[45] In contrast to the large ~360 cm^{-1} gap separating WO_4 stretching and bending modes in the PDOS of α-ZrW_2O_8, strong phonon signatures for the ν_4 antisymmetric bending modes of PO_4 units in $Zr_2(WO_4)(PO_4)_2$ are predicted in this study within ~570−635 cm^{-1}. The calculated $\nu_2(PO_4)$ symmetric bending modes are in the range ~365−425 cm^{-1}, with PO_4 rocking modes predicted at lower wavenumbers within ~182−200 cm^{-1}. The computed ν_3 and ν_1 stretching modes of PO_4 units are within the ranges ~992−1181 cm^{-1} and ~1065−1084 cm^{-1}. In $Zr_2(WO_4)(PO_4)_2$, the computed modes of vibration for WO_4 units are ~990−1040 cm^{-1} for ν_1, ~830−1000 cm^{-1} for ν_3, and bending modes within 245−400 cm^{-1}. While vibrations from WO_4 and PO_4 units are predominant in the PDOS, a finer phonon mode analysis reveals that ZrO_6 vibrations also contribute to the PDOS: $\nu_1(ZrO_6)$ symmetric stretching modes appear combined with $\nu_3(PO_4)$ and $\nu_1(PO_4)$ in the range ~1084−1181 cm^{-1}, ZrO_6 bending occurs within ~239−326 cm^{-1} and ZrO_6 rocking around ~188 cm^{-1}. Noticeable P−O bond stretching also appears *ca.* ~1034−1038 cm^{-1} in combination with $\nu_1(WO_4)$ symmetric stretching modes. Below ~227 cm^{-1}, lattice modes are dominant, either pure or combined with PO_4 or ZrO_6 rocking.

With N = 68 atoms (Z = 4 formula units per unit cell), $Zr_2(WO_4)(PO_4)_2$ exhibits $3N = 204$ degrees of freedom, distributed among 201 non-degenerate optical phonons ($\Gamma_{optical}$) and three acoustic phonons ($\Gamma_{acoustic}$). Acoustic phonons correspond to modes of translation at the Γ-point, namely one longitudinal acoustic mode and two transverse acoustic modes with zero-frequency, which are associated with the irreducible representations (irreps) B_{1u}, B_{1u}, and B_{1u} according to the decomposition $\Gamma_{acoustic}(3) = B_{1u} + B_{2u} + B_{3u}$ of the orthorhombic *Pbcn* space group for $Zr_2(WO_4)(PO_4)_2$ (see character table in Table 3 for space group *Pbcn* with 8*d* and 4*c* Wyckoff sites occupied). The 201 optical modes can be represented as $\Gamma_{optical}(201) = 25A_g + 26B_{1g} + 25B_{2g} + 26B_{3g} + 25A_u + 25B_{1u} + 24B_{2u} + 25B_{3u}$. Among these optical modes, vibrational modes belonging to the B_{1u}, B_{2u}, and B_{3u} irreps are only IR-active modes (linear functions), i.e., $\Gamma_{optical}^{IR}(74) = 25B_{1u} + 24B_{2u} + 25B_{3u}$, while vibrational modes of the A_g, B_{1g}, B_{2g} and B_{3g} irreps are only Raman-active modes (quadratic functions), i.e., $\Gamma_{optical}^{Raman}(102) = 25A_g + 26B_{1g} + 25B_{2g} + 26B_{3g}$, and the remaining 25 vibrational modes belonging to the A_u irrep are both IR- and Raman-inactive modes.

Eigenfrequencies of the most intense infrared- and Raman-active vibrational modes of $Zr_2(WO_4)(PO_4)_2$ calculated from DFPT at the GGA/PBEsol level have been assigned using group theory and are summarized in Table 4. An extensive and systematic comparison has been made with the IR- and Raman-active bands observed in this study (see Figure 4 and Figure 5), along with the recent Raman bands reported by Yuan et al.[41] on samples pre-sintered at 1573 K, which consist of a mixture of $Zr_2(WO_4)(PO_4)_2$ and WO_3. Let us note that bands characteristic of WO_3 at $\omega \cong 711$ and 808 cm^{-1} are not observed in the Raman spectrum of $Zr_2(WO_4)(PO_4)_2$ collected in this study (see Figure 5), therefore confirming the high purity of the samples characterized experimentally.

Table 4. Eigenfrequencies of the Most Intense Infrared- and Raman-Active Vibrational Modes of $Zr_2(WO_4)(PO_4)_2$ (Space Group *Pbcn*, IT No. 60) Calculated from Density Functional Perturbation Theory (DFPT) at the GGA/PBEsol Level. Observed IR- and Raman-Active Bands Are Reported for Comparison.

Irrep.[a]	IR (cm^{-1})		Raman (cm^{-1})			Mode Description[e]
	DFPT[b]	Expt.[b]	DFPT[b]	Expt.[b]	Expt.[c]	
B_{1u}	1181	1197*w*				$\nu_3(PO_4)+\nu_1(ZrO_6)$
B_{2u}	1167	1178*w*				$\nu_3(PO_4)+\nu_1(ZrO_6)$
B_{1g}			1163	1174*w*		$\nu_3(PO_4)+\nu_1(ZrO_6)$
A_g			1084	1096*w*	1097*w*	$\nu_1(PO_4)+\nu_1(ZrO_6)$
B_{2u}	1065	1080*m*				$\nu_1(PO_4)$
B_{1g}			1038			$\nu_1(WO_4)$+P−O stretching
A_g			1034	1039*s*		$\nu_1(WO_4)$+P−O stretching
B_{1u}	1027					$\nu_1(WO_4)+\nu_3(PO_4)$
B_{3g}			1022	1022*s*	1019*s*	$\nu_3(PO_4)$
A_g			1022			$\nu_3(PO_4)+\nu_1(WO_4)$
B_{2g}			1020			$\nu_3(PO_4)$
B_{1u}	1007					$\nu_3(PO_4)+\nu_1(WO_4)$
B_{2u}	1007	1004*s*				$\nu_3(PO_4)$
B_{1u}	1004					$\nu_3(PO_4)$
B_{2g}			1002			$\nu_3(PO_4)$
A_g			1002	1011*s*		$\nu_3(PO_4)+\nu_1(WO_4)$
B_{3g}			999			$\nu_3(PO_4)+\nu_3(WO_4)$
B_{2u}	995					$\nu_3(PO_4)$
B_{3u}	994					$\nu_3(PO_4)$
A_g			992			$\nu_3(PO_4)+\nu_1(WO_4)$
B_{3u}	881					$\nu_3(WO_4)$
B_{2g}			878			$\nu_3(WO_4)$
B_{3g}			874	870*m*	868*m*	$\nu_3(WO_4)$
B_{2u}	874					$\nu_3(WO_4)$
B_{1u}	872	872*s*				$\nu_3(WO_4)$
B_{1g}			837			$\nu_3(WO_4)$
B_{3u}	837	843*s*				$\nu_3(WO_4)$
A_g			835			$\nu_3(WO_4)$
B_{2g}			831	826*s*	830*s*	$\nu_3(WO_4)$
B_{2g}			634			$\nu_4(PO_4)$
B_{2u}	630	640*w*				$\nu_4(PO_4)$
A_g			625	630*w*		$\nu_4(PO_4)$
A_g			595	607*w*		$\nu_4(PO_4)$
A_g			571	582*w*		$\nu_4(PO_4)$
B_{3u}	570	583*w*				$\nu_4(PO_4)$
B_{3g}			422			$\nu_2(PO_4)$
A_g			412	426*w*	425*w*	$\nu_2(PO_4)$
B_{2u}	400					$\nu_2(PO_4)+\nu_2(WO_4)$
A_g			396	408*w*	407*w*	$\nu_2(PO_4)+\nu_2(WO_4)$
B_{1u}	394					$\nu_2(PO_4)+\nu_2(WO_4)$
B_{3u}	366					$\nu_2(PO_4)+\nu_2(WO_4)$
A_g			349	356*w*		$\nu_2(WO_4)$
B_{3u}	349					$\nu_2(WO_4)$
B_{1u}	346					$\nu_2(WO_4)$
B_{2g}			342	346*w*		$\nu_2(WO_4)$
A_g			336			$\nu_2(WO_4)$
B_{3u}	326					Bending(ZrO_6)
B_{1u}	324					Bending(ZrO_6)+$\nu_2(WO_4)$
A_g			322	316*w*		Bending(ZrO_6)+$\nu_2(WO_4)$
B_{1g}			306	303*w*		Bending(ZrO_6)+$\nu_2(WO_4)$
B_{2u}	298					Bending(ZrO_6)+$\nu_2(WO_4)$
A_g			278	272*w*		$\nu_2(WO_4)$
B_{3u}	277					Bending(ZrO_6)
B_{1u}	273					Bending(ZrO_6)+$\nu_2(WO_4)$
B_{3u}	267					$\nu_2(WO_4)$
A_g			246	250*w*		Bending(ZrO_6)+$\nu_2(WO_4)$
B_{1u}	239					Bending(ZrO_6)
B_{3u}	227					Lattice
B_{2g}			200	199*w*		Rocking(PO_4)+Lattice
B_{3u}	188					Rocking(ZrO_6)+Lattice
A_g			182	188*w*		Rocking(PO_4)+Lattice

A_g		162	155*w*	Lattice
A_g		125	128*w*	Lattice

[a] Vibrational modes belonging to the A_g, B_{1g}, B_{2g} and B_{3g} irreps are Raman active (quadratic functions), while modes from the B_{1u}, B_{2u} and B_{3u} irreps are IR active (linear functions). [b] This study; band intensity: *s* = strong *m* = medium, *w* = weak. [c] Yuan et al., 2017; ref. 41. [d] Free tungstate and phosphate ions vibration modes: symmetric (ν_1) and antisymmetric (ν_3) stretching modes, symmetric (ν_2) and antisymmetric (ν_4) bending modes; ZrO_6 octahedral units vibration modes: symmetric (ν_1) and antisymmetric (ν_2 and ν_3) stretching modes; bending and rocking modes are referred to above as bending(ZrO_6) and rocking(ZrO_6).

As shown in Table 4 and Figure 4, the most intense FT-IR bands observed in this study are centered at 1197 cm^{-1} (*w*: weak), 1178 cm^{-1} (*w*), 1080 cm^{-1} (*m*: medium), 1004 cm^{-1} (*s*: strong), 872 cm^{-1} (*s*), 843 cm^{-1} (*s*), 640 cm^{-1} (*w*), and 583 cm^{-1} (*w*). These bands are well reproduced by the IR spectrum simulated using PBEsol, with corresponding bands predicted at 1181 cm^{-1} (*w*) [B_{1u}; $\nu_3(PO_4)+\nu_1(ZrO_6)$], 1167 cm^{-1} (*w*) [B_{2u}; $\nu_3(PO_4)+\nu_1(ZrO_6)$], 1065 cm^{-1} (*m*) [B_{2u}; $\nu_1(PO_4)$], 1007 cm^{-1} (*s*) [B_{2u}; $\nu_3(PO_4)$], 872 cm^{-1} (*s*) [B_{1u}; $\nu_3(WO_4)$], 837 cm^{-1} (*s*) [B_{3u}; $\nu_3(WO_4)$], 630 cm^{-1} (*w*) [B_{2u}; $\nu_4(PO_4)$], and 570 cm^{-1} (*w*) [B_{3u}; $\nu_4(PO_4)$], respectively. The strong IR band observed at 1004 cm^{-1} actually appears to be a combination of three bands predicted at 1007 cm^{-1} [B_{1u}; $\nu_3(PO_4)+\nu_1(WO_4)$], 1007 cm^{-1} [B_{2u}; $\nu_3(PO_4)$], and 1004 cm^{-1} [B_{1u}; $\nu_3(PO_4)$], which are not resolved experimentally. Similarly, the intense band observed at 872 cm^{-1} originates from bands at 872 cm^{-1} [B_{1u}; $\nu_3(WO_4)$] and 874 cm^{-1} [B_{2u}; $\nu_3(WO_4)$]. Graphical representations of the vibration vectors superimposed on the structure of $Zr_2(WO_4)(PO_4)_2$ for the four strong- and medium-intensity IR bands discussed above are provided in Supporting Information. In addition to these intense bands, eighteen new bands have been predicted using DFPT, most of them in the far-IR range (*i.e.*, below ~400 cm^{-1}), at 1027, 995, 994, 881, 400, 394, 366, 349, 346, 326, 324, 298, 277, 273, 267, 239, 227 and 188 cm^{-1} (see Table 4). It is also worth noting that, although $Zr_2(WO_4)(PO_4)_2$ is a NTE material and a frequency shift might be expected between DFPT results obtained at 0 K and IR experiments at room temperature, excellent agreement is achieved between theory and experiment. Therefore, NTE in $Zr_2(WO_4)(PO_4)_2$ appears to have limited impact on the spectral properties of this compound. A similar conclusion was previously reached for the isotropic NTE material α-ZrW_2O_8.[45]

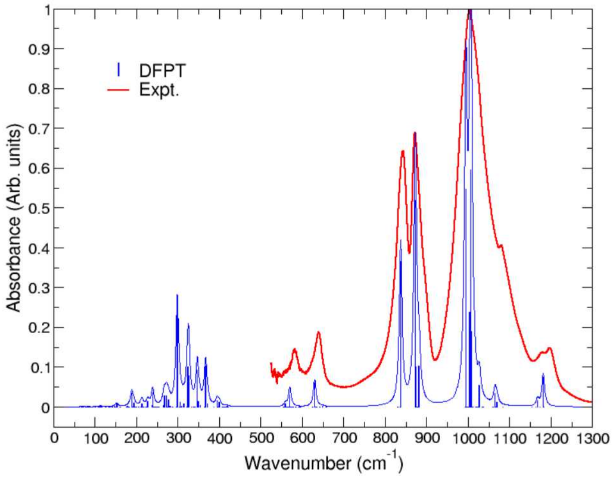

Figure 4. Fourier transform infrared (FT-IR) spectrum of $Zr_2(WO_4)(PO_4)_2$ observed at room temperature (red line), along with the infrared spectrum simulated from density functional perturbation theory (DFPT) at the GGA/PBEsol level (blue line). Natural line broadening was simulated from DFPT eigenfrequencies (vertical blue bars) using a Lorentzian lineshape function with a full width at half maximum (FWHM) of 4 cm^{-1}.

The Raman spectrum of $Zr_2(WO_4)(PO_4)_2$ simulated with DFPT/PBEsol is displayed in Figure 5, along with the Raman data collected in this study at room temperature. Similar to IR results, excellent overall agreement is obtained between DFPT predictions and observation. The computed vibrational eigenfrequencies for the most intense Raman-active modes are summarized in Table 4, together with Raman band centers measured in this study and in the investigation of Yuan et al.[41] In the latter, major Raman bands were centered at 1097 cm^{-1} (*w*), 1019 cm^{-1} (*s*), 868 cm^{-1} (*m*), 830 cm^{-1} (*s*), 425 cm^{-1} (*w*), and 407 cm^{-1} (*w*), with additional bands located at $\omega \cong 711$ and 808 cm^{-1} stemming from the presence of WO_3 in $Zr_2(WO_4)(PO_4)_2$ samples characterized.[41] As shown in Figure 5 and Table 4, these $Zr_2(WO_4)(PO_4)_2$ bands have also been observed in this study at 1096 cm^{-1} (*w*), 1022 cm^{-1} (*s*), 870 cm^{-1} (*m*), 826 cm^{-1} (*s*), 426 cm^{-1} (*w*), and 408 cm^{-1} (*w*). In addition, two new strong Raman bands of $Zr_2(WO_4)(PO_4)_2$ have been identified at 1039 and 1011 cm^{-1}, along with fourteen new weak bands located at 1174, 630, 607, 582, 356, 346, 316, 303, 272, 250, 199, 188, 155 and 128 cm^{-1}. No spectral signatures of WO_3 at 711 and 808 cm^{-1} were observed in the spectrum collected, thus confirming the high-purity of the sample synthesized in this study.

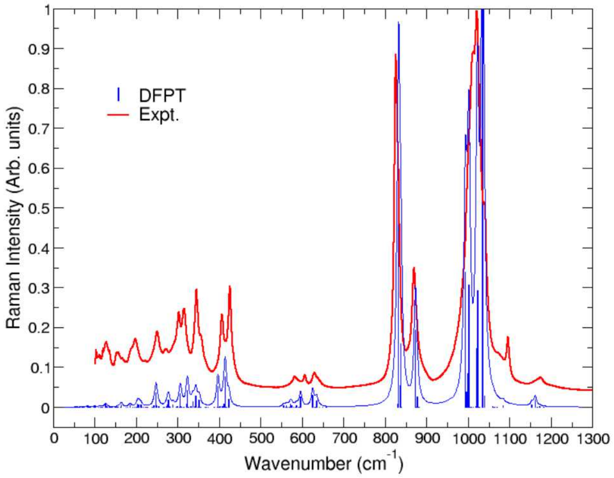

Figure 5. Raman spectrum of $Zr_2(WO_4)(PO_4)_2$ observed at room temperature (red line), along with the Raman spectrum simulated from density functional perturbation theory (DFPT) at the GGA/PBEsol level (blue line). Natural line broadening was simulated from DFPT eigenfrequencies (vertical blue bars) using a Lorentzian lineshape function with a full width at half maximum (FWHM) of 4 cm^{-1}.

As depicted in Figure 5 and Table 4, excellent agreement between the Raman spectrum simulated from DFPT/PBEsol calculations and Raman data. Major strong- and medium-intensity Raman bands were predicted to be at 1034 cm^{-1} (*s*) [A_g; $\nu_1(WO_4)$+P−O stretching], 1022 cm^{-1} (*s*) [B_{3g}; $\nu_3(PO_4)$], 1002 cm^{-1} (*s*) [A_g; $\nu_3(PO_4)+\nu_1(WO_4)$], 874 cm^{-1} (*m*) [B_{3g}; $\nu_3(WO_4)$], and 831 cm^{-1} (*s*) [B_{2g}; $\nu_3(WO_4)$]. Graphical representations of the vibration vectors superimposed on the structure of $Zr_2(WO_4)(PO_4)_2$ for these strong- and medium-intensity Raman bands are given in Supporting Information. Based on DFPT calculations (see Table 4), some of the bands observed in this study appear to result from combinations of bands, i.e., the bands collected at 1039 cm^{-1} (*s*), 1022 cm^{-1} (*s*), 1011 cm^{-1} (*s*), 870 cm^{-1} (*m*), 826 cm^{-1} (*s*), 426 cm^{-1} (*w*), and 346 cm^{-1} (*w*) are actually combinations of bands at 1038 cm^{-1} (B_{1g}) + 1034 cm^{-1} (A_g), 1022 cm^{-1} (B_{3g}) + 1022 cm^{-1} (A_g) + 1020 cm^{-1} (B_{2g}), 1002 cm^{-1} (B_{2g}) + 1002 cm^{-1} (A_g) + 999 cm^{-1} (B_{3g}), 878 cm^{-1} (B_{2g}) + 874 cm^{-1} (B_{3g}), 835 cm^{-1} (A_g) + 831 cm^{-1} (B_{2g}), 422 cm^{-1} (B_{3g}) + 412 cm^{-1} (A_g), and 342 cm^{-1} (B_{2g}) + 336 cm^{-1} (A_g), respectively. The fourteen new weak bands observed above have been successfully confirmed and assigned using DFPT calculations, with band centers predicted at 1163, 625, 595, 571, 349, 342, 322, 306, 278, 246, 200, 182, 162 and 125 cm^{-1}. A detailed assignment (irreps and modes description) of these new bands based in DFTP calculations is reported in Table 4.

4. CONCLUSION

DFT/DFPT calculations were carried out at the GGA/PBEsol level of theory to extensively investigate the relationship between the crystal structure and vibrational properties of NTE crystalline $Zr_2(WO_4)(PO_4)_2$ and its phonon DOS, IR and Raman spectra. The accuracy of predictions using DFT/DFPT methods was successfully assessed and validated by systematic comparison with experimental FT-IR and Raman data collected in this study and previous investigations. The excellent agreement achieved between DPFT calculations at 0 K and spectroscopic measurements at room temperature suggests that negative thermal expansion in $Zr_2(WO_4)(PO_4)_2$ has a very limited impact on the spectral properties of this compound.

Based on combined first-principles and experimental approaches, new comprehensive and extensive assignments have been made for the spectra of $Zr_2(WO_4)(PO_4)_2$, resulting in the characterization of its 29 and 34 most intense IR- and Raman-active modes, respectively. In addition, these DFPT results also showed that $\nu_1(PO_4)$ symmetric stretching and $\nu_3(PO_4)$ antisymmetric stretching bands were interchanged in previous tentative band assignments of Raman experiments by Yuan et al. This conclusion is also supported by existing vibrational spectroscopy characterization of zirconium phosphate minerals/ceramics, indicating higher frequency for $\nu_3(PO_4)$ bands compared to $\nu_1(PO_4)$ bands.

The IR spectrum simulated using DFPT/PBEsol predicts bands at 1181 cm^{-1} (*w: weak*) [B_{1u}; $\nu_3(PO_4)+\nu_1(ZrO_6)$], 1167 cm^{-1} (*w*) [B_{2u}; $\nu_3(PO_4)+\nu_1(ZrO_6)$], 1065 cm^{-1} (*m: medium*) [B_{2u}; $\nu_1(PO_4)$], 1007 cm^{-1} (*s: strong*) [B_{2u}; $\nu_3(PO_4)$], 872 cm^{-1} (*s*) [B_{1u}; $\nu_3(WO_4)$], 837 cm^{-1} (*s*) [B_{3u}; $\nu_3(WO_4)$], 630 cm^{-1} (*w*) [B_{2u}; $\nu_4(PO_4)$], and 570 cm^{-1} (*w*) [B_{3u}; $\nu_4(PO_4)$], which accurately reproduce the most intense FT-IR bands observed in this study. Calculations also show that some of the IR bands observed correspond to combination of multiple bands, which cannot be resolved experimentally.

In addition to these bands, eighteen new IR bands − most of them in the far-IR range − were predicted using DFPT at 1027, 995, 994, 881, 400, 394, 366, 349, 346, 326, 324, 298, 277, 273, 267, 239, 227 and 188 cm^{-1}.

Strong- and medium-intensity Raman bands were predicted with DFPT/PBEsol at 1034 cm^{-1} (*s*) [A_g; $\nu_1(WO_4)$+P−O stretching], 1022 cm^{-1} (*s*) [B_{3g}; $\nu_3(PO_4)$], 1002 cm^{-1} (*s*) [A_g; $\nu_3(PO_4)+\nu_1(WO_4)$], 874 cm^{-1} (*m*) [B_{3g}; $\nu_3(WO_4)$], and 831 cm^{-1} (*s*) [B_{2g}; $\nu_3(WO_4)$], which accurately matched all the band centers observed in present and past Raman experimental characterizations. In this study, two new strong Raman bands of $Zr_2(WO_4)(PO_4)_2$ were identified at 1039 and 1011 cm^{-1}, along with fourteen new weak bands located at 1174, 630, 607, 582, 356, 346, 316, 303, 272, 250, 199, 188, 155 and 128 cm^{-1}. No spectral signatures of WO_3 at 711 and 808 cm^{-1} were observed, thus confirming the high-purity of the sample synthesized in this study using hydrothermal methods. DFPT calculations showed that some of the Raman bands observed at 1039 cm^{-1} (*s*), 1022 cm^{-1} (*s*), 1011 cm^{-1} (*s*), 870 cm^{-1} (*m*), 826 cm^{-1} (*s*), 426 cm^{-1} (*w*), and 346 cm^{-1} (*w*) originate from combinations of bands. DFPT calculations predicted Raman-active bands at 1163, 625, 595, 571, 349, 342, 322, 306, 278, 246, 200, 182, 162 and 125 cm^{-1}, which coincide with the fourteen new weak Raman bands observed.

A detailed and extensive assignment, including irreps and modes description, of the most intense IR- and Raman-active bands was made based on DFTP calculations and the corresponding graphical representations of the vibration vectors for atomic motion in the $Zr_2(WO_4)(PO_4)_2$ structure were provided for the strongest IR and Raman bands.

The DFT/DFPT results presented in this investigation demonstrated the high accuracy of the PBEsol exchange-correlation functional for studying the correlation between vibrational and spectroscopic properties of crystalline materials using first-principles methods, in particular to describe the structure-property relationships for the class of materials exhibiting NTE properties.

ASSOCIATED CONTENT

Supporting Information

Graphical representations of the vibration vectors superimposed on the structure of $Zr_2(WO_4)(PO_4)_2$ for the strong- and medium-intensity IR and Raman bands.

AUTHOR INFORMATION

Corresponding Author

*E-mail pfweck@sandia.gov; Ph 505-844-8144 (P.F.W.).

ORCID

Philippe F. Weck: 0000-0002-7610-2893
Eunja Kim: 0000-0002-3079-9680
Jeffery A. Greathouse: 0000-0002-4247-3362

Notes

The authors declare no competing financial interests.

ACKNOWLEDGMENT

Sandia National Laboratories is a multi-mission laboratory managed and operated by National Technology and Engineering Solutions of Sandia, LLC., a wholly owned subsidiary of Honeywell International, Inc., for the U.S. Department of Energy's National Nuclear Security Administration under Contract DE-NA0003525. This work was supported by Laboratory Directed Research and Development (LDRD) funding from Sandia National Laboratories. This work was performed, in part, at the Center for Integrated Nanotechnologies, an Office of Science User Facility operated for the U.S. Department of Energy (DOE) Office of Science. The views expressed in the article do not necessarily represent the views of the U.S. DOE or the United States Government.

REFERENCES

---

[1] Korthuis, V.; Khosrovani, N.; Sleight, A. W.; Roberts, N.; Dupree, R.; Warren, W. W. Negative Thermal Expansion and Phase Transitions in the $ZrV_{2-x}P_xO_7$ Series. *Chem. Matter*. **1995**, *7*, 412.

[2] Auray, M.; Quarton, M.; Leblanc, M. Zirconium Tungstate. *Acta Crystallogr. C* **1995**, *51*, 2210-2213.

[3] Mary, T. A.; Evans, J. S. O.; Sleight, A. W.; Vogt, T. Negative Thermal Expansion from 0.3 to 1050 Kelvin in ZrW_2O_8. *Science* **1996**, *272*, 90-92.

[4] Evans, J. S. O.; Mary, T. A.; Vogt, T.; Subramanian, M. A.; Sleight, A. W. Negative Thermal Expansion in ZrW_2O_8 and HfW_2O_8. *Chem. Mater.* **1996**, *8*, 2809-2823.

[5] Evans, J. S. O.; Hu, Z.; Jorgensen, J. D.; Argyriou, D. N.; Short, S.; Sleight, A. W. Compressibility, Phase Transitions, and Oxygen Migration in Zirconium Tungstate, ZrW_2O_8. *Science* **1997**, *275*, 61-65.

[6] Evans, J. S. O.; David, W. I. F., Sleight, A. W. Structural Investigation of the Negative-Thermal-Expansion Material ZrW_2O_8. *Acta Crystallogr.B* **1999**, *55*, 333-340.

[7] Ernst, G.; Broholm, C.; Kowach, G. R.; Ramirez, A. P. Phonon density of states and negative thermal expansion in ZrW_2O_8. *Nature* **1998**, *396*, 147-149.

[8] David, W. I. F.; Evans, J. S. O.; Sleight, A. W. Direct Evidence for a Low-Frequency Phonon Mode Mechanism in the Negative Thermal Expansion Compound ZrW_2O_8. *Europhys. Lett.* **1999**, *46*, 661-666.

[9] Perottoni, C.A.; da Jornada, J.A.H. Pressure-Induced Amorphization and Negative Thermal Expansion in ZrW_2O_8. *Science* **1998**, *280*, 886-889.

[10] Ramirez, A. P.; Kowach, G. Large Low Temperature Specific Heat in the Negative Thermal Expansion Compound ZrW_2O_8. *Phys. Rev. Lett.* **1998**, *80*, 4903-4906.

[11] Yamamura, Y.; Nakajima, N.; Tsuji, T. Heat Capacity Anomaly Due to the α to β Structural Phase Transition in ZrW_2O_8. *Solid. State Commun.* **2000**, *114*, 453–455.

[12] Ravindran, T. R.; Arora, A. K.; Mary, T. A. High Pressure Behavior of ZrW_2O_8: Grüneisen Parameter and Thermal Properties. *Phys. Rev. Lett.* **2000**, *84*, 3879.

[13] Ravindran, T. R.; Arora, A. K.; Mary, T. A. High-Pressure Raman Spectroscopic Study of Zirconium Tungstate. *J. Phys: Condens. Matter* **2001**, *13*, 11573-11588.

[14] Drymiotis, F. R.; Ledbetter, H.; Betts, J. B.; Kimura, T.; Lashley, J. C., Migliori, A.; Ramirez, A.; Kowach, G.; Van Dujin, J. Monocrystal Elastic Constants of the Negative-Thermal-Expansion Compound Zirconium Tungstate (ZrW_2O_8). *Phys. Rev. Lett.* **2004**, *93*, 025502.

[15] Hancock, J. N.; Turpen, C.; Schlesinger, Z.; Kowach, G. R.; Ramirez, A. P. Unusual Low-Energy Phonon Dynamics in the Negative Thermal Expansion Compound ZrW_2O_8. *Phys. Rev. Lett.* **2004**, *93*, 225501.

[16] Keen, D. A.; Goodwin, A. L.; Tucker, M. G.; Dove, M. T.; Evans, J. S. O.; Crichton, W. A.; Brunelli, M. Structural Description of Pressure-Induced Amorphization in ZrW_2O_8. *Phys. Rev. Lett.* **2007**, *98*, 225501.

[17] Bridges, F.; Keiber, T.; Juhas, P.; Billinge, S. J. L.; Sutton, L.; Wilde, J.; Kowach, G. R. Local Vibrations and Negative Thermal Expansion in ZrW_2O_8. *Phys. Rev. Lett.* **2014**, *112*, 045505.

[18] Stevens, R.; Linford, J.; Woodfield, B. F.; Boerio-Goates, J.; Lind, C.; Wilkinson, A. P.; Kowach, G. Heat Capacities, Third-Law Entropies and Thermodynamic Functions of the Negative Thermal Expansion Materials, Cubic a-ZrW_2O_8 and Cubic $ZrMo_2O_8$, From T = (0 to 400 K). *J. Chem. Thermo*. **2003**, *35*, 919–937.

[19] Chu, C. N.; Saka, N.; Suh, N. P. Negative Thermal Expansion Ceramics: A Review. *Mater. Sci. Eng.* **1987**, *95*, 303–308.

[20] Roy, R.; Agrawal, D. K.; McKinstry, H. A. Very Low Thermal Expansion Coefficient Materials. *Ann. Rev. Matter. Sci*. **1989**, *19*, 59–81.

[21] White, G. K. Solids: Thermal Expansion and Contraction. *Contemp. Phys*. **1993**, *34*, 193.

[22] Sleight, A. W. Isotropic Negative Thermal Expansion. *Ann. Rev. Matter. Sci.* **1998**, *28*, 29–43.

[23] Evans, J. S. O. Negative Thermal Expansion Materials. *J. Chem. Soc. Dalton Trans.* **1999**, 3317–3326.

[24] Barrera, G. D.; Bruno, J. A. O.; Barron, T. H. K.; Allan, N. L. Negative Thermal Expansion. *J. Phys.: Condens. Matter* **2005**, *17*, R217.

[25] Takenaka, K. Negative Thermal Expansion Materials: Technological Key for Control of Thermal Expansion. *Sci. Technol. Adv. Mater*. **2012**, *13*, 013001.

[26] Lind, C. Two Decades of Negative Thermal Expansion Research: Where Do We Stand? *Materials* **2012**, *5*, 1125– 1154.

[27] Dove, M. T.; Fang, H. Negative Thermal Expansion and Associated Anomalous Physical Properties: Review of the Lattice Dynamics Theoretical Foundation. *Rep. Prog. Phys.* **2016**, *79*, 066503.

[28] Martinek, C. A.; Hummel, F. A. Subsolidus Equilibria in the System ZrO_2-WO_3-P_2O_5. *J. Am. Ceram. Soc*. **1970**, *53*, 159.

[29] Tsvigunov, A. N.; Sirotinkin, V. P. Synthesis and Results of Indicating of $Zr_2WO_4(PO_4)_2$ X-Ray-Films. *Zhurnal Neorganicheskoi Khimii* **1990**, *35*, 3065.

[30] Evans, J. S. O.; Mary, T. A.; Sleight, A. W. Structure of $Zr_2(WO_4)(PO_4)_2$ from Powder X-Ray Data: Cation Ordering with No Superstructure. *J. Sol. State Chem.* **1995**, *120*, 101.

[31] Evans, J. S. O.; Mary, T. A.; Sleight, A. W. Negative Thermal Expansion in a Large Molybdate and Tungstate Family. *J. Sol. State Chem.* **1997**, *133*, 580.

[32] Isobe, T.; Umezome, T.; Kameshima, Y.; Nakajima, A.; Okada, K. Preparation and Properties of Negative Thermal Expansion $Zr_2WP_2O_{12}$ Ceramics, *Mater. Res. Bull.* **2009**, *44*, 2045.

[33] Cetinkol, M.; Wilkinson, A. P. Pressure Dependence of Negative Thermal Expansion in $Zr_2(WO_4)(PO_4)_2$. *Sol. State Commun*. **2009**, *149*, 421.

[34] Shang, R.; Hu, Q.; Liu, X.; Liang, E.; Yuan, B.; Chao, M. Effect of MgO and PVA on the Synthesis and Properties of Negative Thermal Expansion Ceramics of $Zr_2(WO_4)(PO_4)_2$. *Int. J. Appl. Ceram. Technol*. **2013**, *10*, 849.

[35] Liu, X.; Wang, J.; Fan, C.; Shang, R.; Cheng, F.; Yuan, B.; Song, W.; Chen, Y.; Liang, E.; Chao, M. Control of Reaction Pathways for Rapid Synthesis of Negative Thermal Expansion Ceramic $Zr_2P_2WO_{12}$ with Uniform Microstructure. *Int. J. Appl. Ceram. Technol*. **2015**, *12*, E28.

[36] Shi, X.; Lian, H.; Qi, R.; Cui, L.; Yao, N. Preparation and Properties of Negative Thermal Expansion $Zr_2P_2WO_{12}$ Powders and $Zr_2P_2WO_{12}$/TiNi Composites. *Mater. Sci. Eng. B* **2016**, *203*, 1-6.

[37] Isobe, T.; Kato, Y.; Mizutani, M.; Ota, T.; Daimon, K. Pressureless Sintering of Negative Thermal Expansion ZrW_2O_8/$Zr_2WP_2O_{12}$ Composites. Mater. Lett. **2008**, *62*, 3913.

[38] Tani, J.; Takahashi, M.; Kido, H. Fabrication and Thermal Expansion Properties of ZrW_2O_8/$Zr_2WP_2O_{12}$ Composites. *J. Euro. Ceram. Soc.* **2010**, *30*, 1483.

[39] Yanase, I.; Sakai, H.; Kobayashi, H. Fabrication of $Zr_2WP_2O_{12}$/$ZrV_{0.6}P_{1.4}O_7$ Composite with a Nearly Zero-Thermal-Expansion Property. Mater. Lett. **2017**, *207*, 221.

[40] Cetinkol, M.; Wilkinson, A. P; Lind, C. In Situ High-Pressure Synchrotron X-Ray Diffraction Study of $Zr_2(WO_4)(PO_4)_2$ up to 16 GPa. *Phys. Rev.* B **2009**, *79*, 224118.

[41] Yuan, B. H.; Chen, Y. G.; Zhang, Q. L.; Chen, L. L.; Liu, X. S. Avoiding the Intermediate phase $Zr_2WP_2O_{12}$ to Develop a Larger-Negative-Thermal-Expansion-Coefficient Material $Zr_2W_2P_2O_{15}$. Ceramics Inter. **2017**, *43*, 6831.

[42] Weck, P. F.; Kim, E.; Gordon, M. E.; Greathouse, J. A.; Dingreville, R.; Bryan, C. R. Density Functional Perturbation Theory Analysis of Negative Thermal Expansion $Zr_2(WO_4)(PO_4)_2$. *ACS Omega* **2018**, *3*, 15780.

[43] Perdew, J. P.; Ruzsinszky, A.; Csonka, G. I.; Vydrov, O. A.; Scuseria, G. E.; Constantin, L. A.; Zhou, X.; Burke, K. Restoring the Density-Gradient Expansion for Exchange in Solids and Surfaces. *Phys. Rev. Lett.* **2008**, *100*, 136406.

[44] Weck, P. F.; Kim, E.; Greathouse, J. A.; Gordon, M. E.; Bryan, C. R. Assessing Exchange-Correlation Functionals for Elasticity and Thermodynamics of α-ZrW_2O_8: A Density Functional Perturbation Theory Study. *Chem. Phys. Lett.* **2018**, *698*, 195.

[45] Weck, P. F.; Gordon, M. E.; Greathouse, J. A.; Bryan, C. R.; Meserole, S. P.; Payne, C.; Rodriguez, M. A.; Kim, E. Infrared and Raman Spectroscopy of α-ZrW_2O_8: A Comprehensive Density Functional

---

Perturbation Theory and Experimental Study. *J. Raman Spectro*. **2018**, *49*, 1373.

[46] Gonze, X.; Lee, C. Dynamical matrices, Born effective charges, dielectric permittivity tensors, and interatomic force constants from density-functional perturbation theory. *Phys. Rev. B* **1997**, *55*, 10355.

[47] Weck, P. F.; Kim, E. Assessing Hubbard-Corrected AM05+U and PBEsol+U Density Functionals for Strongly Correlated Oxides CeO_2 and Ce_2O_3. *Chem. Phys. Phys. Chem*. **2016**, *18*, 26816-26826.

[48] Weck, P. F.; Kim, E. Uncloaking the Thermodynamics of the Studtite to Metastudtite Shear-Induced Transformation. *J. Phys. Chem. C* **2016**, *120*, 16553-16560.

[49] Weck, P. F.; Kim, E.; Tikare, V.; Mitchell, J. A. Mechanical Properties of Zirconium Alloys and Zirconium Hydrides Predicted from Density Functional Perturbation Theory. *Dalton Trans*. **2015**, *44*, 18769-18779.

[50] Johnson, T. J.; Sweet, L. E.; Meier, D. E.; Mausolf, E. J.; Kim, E.; Weck, P. F.; Buck, E. C.; McNamara, B. K. Time-Resolved Infrared Reflectance Studies of the Dehydration-Induced Transformation of Uranyl Nitrate Hexahydrate to the Trihydrate Form. *J. Phys. Chem. A* **2015**, *119*, 9996-10006.

[51] Weck, P. F.; Kim E. Layered uranium(VI) hydroxides: structural and thermodynamic properties of dehydrated schoepite α-$UO_2(OH)_2$. *Dalton Trans.* **2014**, *43*, 17191.

[52] Weck, P. F.; Kim E. Solar Energy Storage in Phase Change Materials: First-Principles Thermodynamic Modeling of Magnesium Chloride Hydrates. *J. Phys. Chem. C* **2014**, *118*, 4618.

[53] Kresse, G.; Furthmüller, J. Efficient Iterative Schemes for Ab Initio Total-Energy Calculations Using a Plane-Wave Basis Set. *Phys. Rev.* B **1996**, *54*, 11169-11186.

[54] Blöchl, P. E. Projector Augmented-Wave Method. *Phys. Rev.* B **1994**, *50*, 17953-17979.

[55] Kresse, G.; Joubert, D. From Ultrasoft Pseudopotentials to the Projector Augmented-Wave Method. *Phys. Rev.* B **1999**, *59*, 1758-1775.

[56] Davidson, E. R. *Methods in Computational Molecular Physics*, G. H. F. Diercksen and S. Wilson, Eds., Vol. 113, NATO Advanced Study Institute, Series C, Plenum, New York, 1983, p. 95.

[57] Monkhorst, H. J.; Pack, J. D. Special Points for Brillouin-Zone Integrations. *Phys. Rev.* B **1976**, *13*, 5188-5192.

[58] Colmenero, F.; Bonales, L.J.; Cobos, J.; Timon, V. Thermodynamic and Mechanical Properties of the Rutherfordine Mineral Based on Density Functional Theory. *J. Phys. Chem. C* **2017**, *121*, 5994-6001.

[59] Weck, P. F.; Kim, E.; Buck, E. C. On the Mechanical Stability of Uranyl Peroxide Hydrates: Implications for Nuclear Fuel Degradation. *RSC Adv*. **2015**, *5*, 79090-79097.

[60] Weck, P. F.; Kim, E.; Jove-Colon, C. F. Relationship Between Crystal Structure and Thermo-Mechanical Properties of Kaolinite Clay: Beyond Standard Density Functional Theory. *Dalton Trans*. **2015**, *44*, 12550-12560.

[61] Weck, P. F.; Kim, E. Thermodynamics of Technetium: Reconciling Theory and Experiment Using Density Functional Perturbation Analysis. *Dalton Trans*. **2015**, *44*, 12735-12742.

[62] Colmenero, F.; Fernandez, A. M.; Cobos, J.; Timon, V. Periodic DFT Study of the Thermodynamic Properties and Stability of Schoepite and Metaschoepite Mineral Phases. *ACS Earth and Space Chemistry* **2019**, *3*, 17.

[63] Kirkegaard, M. C.; Langford, J.; Steill, J.; Anderson, B.; Miskowiec, A. Vibrational properties of anhydrous and partially hydrated uranyl fluoride. *J. Chem. Phys*. **2017**, *146*, 024502.

[64] Kirkegaard, M. C.; Niedziela, J. L.; Miskowiec, A.; Shields, A. E.; Anderson, B. B. Elucidation of the Structure and Vibrational Spectroscopy of Synthetic Metaschoepite and Its Dehydration Product. *Inorg. Chem.* **2019**, *58*, 7310.

[65] Liang, E. J; Liang, Y. Zhao, Y.; Liu, J. Jiang, Y. Low-Frequency Phonon Modes and Negative Thermal Expansion in A(MO4)2 (A = Zr, Hf and M = W, Mo) by Raman and Terahertz Time-Domain Spectroscopy. *J. Phys. Chem. A* **2008**, *112*, 12582.

[66] Bohre, A.; Awasthi, K. Immobilization of Radioactive Waste in Ceramic Based Hosts: Radioactive Waste Immobilization. Anchor Academic Publishing, Hamburg, 2014.

[67] Frost, R. L.; Scholz, R.; Lopez, A.; Xi, Y. F. A vibrational Spectroscopic Study of the Phosphate Mineral Whiteite $CaMn^{++}Mg_2Al_2(PO_4)_4(OH)_2.8(H_2O)$. *Spectrochim. Acta A - Molec. Biomed. Spectro*. **2014**, *124*, 243.